Atomic Force Microscopy Study of Discrete Dislocation Pile-ups at Grain Boundaries in Bi-Crystalline Micro-Pillars

Xiaolei Chen, Thiebaud Richeton, Christian Motz, Stéphane Berbenni

crystals

MDPI

Article

Atomic Force Microscopy Study of Discrete Dislocation Pile-ups at Grain Boundaries in Bi-Crystalline Micro-Pillars

Xiaolei Chen [1,2], Thiebaud Richeton [1,*], Christian Motz [2] and and Stéphane Berbenni [1]

[1] Université de Lorraine, CNRS, Arts et Métiers ParisTech, LEM3, F-57000 Metz, France; xiaolei.chen@univ-lorraine.fr (X.C.); stephane.berbenni@univ-lorraine.fr (S.B.)

[2] Department of Materials Science and Engineering, Saarland University, 66123 Saarbrücken, Germany; motz@matsci.uni-sb.de

* Correspondence: thiebaud.richeton@univ-lorraine.fr; Tel.: +33-372747802

Received: 20 April 2020; Accepted: 18 May 2020; Published: 20 May 2020

Abstract: Compression tests at low strains were performed to theoretically analyze the effects of anisotropic elasticity, misorientation, grain boundary (GB) stiffness, interfacial dislocations, free surfaces, and critical force on dislocation pile-ups in micro-sized Face-Centered Cubic (FCC) Nickel (Ni) and α-Brass bi-crystals. The spatial variations of slip heights due to localized slip bands terminating at GB were measured by Atomic Force Microscopy (AFM) to determine the Burgers vector distributions in the dislocation pile-ups. These distributions were then simulated by discrete pile-up micromechanical calculations in anisotropic bi-crystals consistent with the experimentally measured material parameters. The computations were based on the image decomposition method considering the effects of interphase GB and free surfaces in multilayered materials. For Ni and α-Brass, it was found that the best predicted step height spatial profiles were obtained considering anisotropic elasticity, free surface effects, a homogeneous external stress and a certain critical force in the material to equilibrate the dislocation pile-ups.

Keywords: micromechanical testing; micro-pillar; bi-crystal; discrete dislocation pile-up; grain boundary; free surface; anisotropic elasticity; crystallographic slip

1. Introduction

The plasticity of crystalline materials results primarily from motion and multiplication of dislocations. Both theoretical and experimental investigations show that the mechanical properties of metals depend on the density, the distribution, the nucleation, and the mobility of dislocations. In particular, the mechanical properties of polycrystals depend on the presence of grain boundaries (GBs), such as the elastic limit and strain hardening. More specifically, these properties are greatly dependent on the interaction mechanisms between dislocations and GBs (dislocation transmission or absorption at GB, formation of a dislocation pile-up, etc.). Indeed, GBs generally present themselves as obstacles to dislocation motion.

In the case of grain size reduction, which means the increase of GB fraction in the material, the material strength is increased following the Hall–Petch's relationship [1–3]. Experimental observations of collective dislocation distributions in the neighborhood of GBs have also made it possible to characterize slip lines using electron microscopy. The interaction between dislocations and GB can be directly observed through in-situ mechanical tests in a Transmission Electron Microscope (TEM). From TEM, it is also possible to obtain the position of each dislocation in a discrete dislocation pile-up, which can be used to calculate stress concentrations at GB [4]. Electron Back Scattered Diffraction (EBSD) measurements in Scanning Electron Microscopes (SEM)

are able to measure the local crystallographic orientations during deformation and therefore the evolution of intra-granular lattice rotations and geometrically dislocation densities [5,6]. Moreover, the coupling of Electron Channelling Contrast Imaging (ECCI) and EBSD permits characterizing single dislocations, dislocation densities, and dislocation substructures in deformed bulk materials [7]. Recently, Atomic Force Microscopy (AFM) makes it possible to analyze the topography and surface roughness of a material following the emergence of dislocations (slip step heights) during mechanical loading of single and poly-crystals [8–10]. Moreover, based on experimental observations, multi-scale simulations involving Crystal Plasticity Finite Element Method (CPFEM), Discrete Dislocation Dynamics (DDD), and Molecular Dynamics (MD) have been developed during these last decades. These methods aim at deeply understanding slip mechanisms and the interactions between dislocations and GBs, and to predict mechanical properties of crystalline materials. However, CPFEM can only consider averaged slip in continuum mechanics, which cannot be used to investigate the discrete interactions between dislocations and GBs. DDD can be performed to study the motion of each individual dislocation, but the complex properties of GBs are missing in this method and elastic anisotropy calculations remain tedious. MD can show the precise structure of dislocation cores and GBs at atomic scale, but it can be only used for simulations at the nanoscale and within a small period of time due to intensive required computing resources.

As the simplest system containing GB, the bi-crystal configuration has been extensively studied. Dehm et al. [11] have reported a comprehensive review on micro-/nanomechanical testing at small scale, especially about GB effect in plasticity and the interactions between dislocations and GBs. Based on many experimental results, there are mainly four mechanisms of dislocation-GB interactions which have been studied: dislocation transmission across GB [12], GB as a dislocation source for lattice dislocation [13], formation of a dislocation pile-up [4] and dislocation absorption at GB [14]. The dislocation transmission is largely investigated through the geometrical transmission factor as reviewed by Bayerschen et al. [15] and the critical stress for transmission as reviewed by Hunter et al. [16]. The geometrical transmission factor has been firstly proposed by Livingston and Chalmers [17] considering only slip system orientations. Then, Shen et al. [4] have proposed another transmission factor considering both slip systems and GB orientations, which has been successfully applied to the prediction of slip activity due to a dislocation pile-up in a 304 stainless steel. Afterwards, Beyerlein et al. [18] have proposed another transmission factor considering threshold angles for the slip systems and GB. It is conjectured that the slip transfer is not possible if at least one of these two angles is bigger than a critical angle [18,19]. The critical transmission stress is generally studied based on image force on dislocations due to the moduli mismatch [20–24]. Furthermore, the interaction between dislocations and special boundaries like twin boundaries has been investigated by many researchers [25–28]. As discussed above, it is believed that a critical stress is needed for the dislocation to get from one grain to the other grain across the GB. The GB will dominate the overall material's behavior when this critical stress is higher than the size-dependent single crystalline flow stress. However, Imrich et al. [25] have showed that, at a critical small sample size, the coherent Σ3 twin GB may not have an impact on the overall mechanical property of micro-beam since the critical stress for transmission is quite low in this case, as shown also by Malyar et al. [28]. In general, however, a large angle random GB does have an evident influence on slip transmission mechanism [29].

In this study, the objective is to develop a new experimental/theoretical methodology suitable for investigating the effects of elastic and plastic anisotropies on the interactions between dislocations and GBs in bi-crystalline micro-pillars. We will consider the effects of GB stiffness, free surfaces, and critical force (lattice friction force and other forces due to obstacles to dislocation motion) on discrete dislocation pile-ups at grain boundaries. In order to reach this objective, both an experimental study based on compression tests on bi-crystalline micro-pillars and a theoretical investigation of discrete dislocation pile-ups in heterogeneous and anisotropic media are performed. Among the different possible mechanisms involving collective dislocation behavior, dislocation pile-ups at GBs and slip transfer are essentially studied. The experimental procedure of in-situ micro-compression

tests on Nickel (Ni) and α-Brass bi-crystals is first described in Section 2. Then, slip line height profiles analyzed by SEM and AFM are presented in Section 3. Moreover, the simulation of the slip step height profiles using an anisotropic and heterogeneous discrete dislocation pile-up model in a bi-crystalline configuration are given in Section 4. All the simulation results and the important material parameters for both Ni and α-Brass samples are discussed. Section 5 provides the conclusions.

2. Experiments

2.1. Materials

The materials used for bi-crystalline micro-pillars are Ni with very high purity (99.999%) and α-Brass (70%Cu-30%Zn, wt%) with impurities (Fe, Pb, P and As, etc.) less than 0.001%. The elastic stiffness constants of Ni are $C_{11} = 246.5$ GPa, $C_{12} = 147.3$ GPa, $C_{44} = 124.7$ GPa [30] and those of α-Brass are $C_{11} = 139.21$ GPa, $C_{12} = 104.51$ GPa, $C_{44} = 71.3$ GPa [31,32]. Thus, these two materials have an elastic anisotropy Zener ratio $A = 2C_{44}/(C_{11} - C_{12})$ of the order of 2.51 and 4.11, respectively. Furthermore, the stacking fault energies for α-Brass and Ni are about 14 mJ/m^2 [33] and 90 mJ/m^2 [34], respectively. The stacking fault energy of α-Brass is low which promotes planar slip and thus facilitates the observation of localized slip. Although the stacking fault energy of Ni is higher, planar slip was still well observed in Ni bi-crystals during compression tests [35].

2.2. Sample Preparation and Characterization

Macrosamples were prepared in the form of cubes of $20 \times 20 \times 5$ mm^3. These macrosamples were ground with grit paper and then homogenized by heat treatment. For Ni, the produced samples were homogenized at 1100 °C for three days in vacuum. However, for α-Brass, in order to prevent dezincified phenomenon in vacuum [36], the heat treatment was realized in argon at 980 °C for 1 min with a special sample holder. Then, the samples were ground again and polished using a diamond suspension of particle sizes until 1 micron on zeta cloth. After that, the sample surfaces were finally polished by OP-U-NonDry solution with water on chem-cloth for 5 mins. At the end, the samples were electropolished at a voltage of 24 V for 20 s with electrolyte A2 (65∼86% Ethanol, 10∼15% 2-Butoxyethanol and 5∼15% water) for Ni and with electrolyte D2 (15∼35% Phosphoric acid, 15∼25% Ethanol, <10% Propane-1-OL, <1% urea and 50∼70% water) for α-Brass in order to eliminate hardening and damage (including scratches) occurred during the mechanical polishing.

Each grain orientation was measured by EBSD (Oxford, UK) in a Carl Zeiss SIGMA series SEM (Oberkochen, Germany). Orientation maps were acquired with a 20 kV acceleration voltage and a spatial step size of 20 µm. Data processing was performed by Flamenco Channel 5 software (HKL Technology, Oxford Instruments, Abingdon, UK) with the indexing rate always greater than 99%. In order to investigate dislocation pile-ups behavior and their interaction with GBs by AFM measurements and slip lines characterization on the upper surface, special GBs were chosen from the hereinafter described conditions following the surface notations presented in Figure 1b,d. The first condition is that GB is roughly perpendicular to the upper surface. The second one is that with a mechanical loading parallel to GB plane, for the target grain, the Burgers vector of the likely activated slip system (i.e., the one with the maximum Schmid factor) must not be perpendicular to GB. Meanwhile, the slip plane of this slip system must not be parallel to the upper surface. These conditions ensure that the Burgers vector has a component perpendicular to the upper surface where AFM measurements will be performed. Based on all the above conditions, one GB of each material was used to analyze the dislocation distributions and the slip transmission phenomenon.

2.3. Micro-Pillar Production

The chosen GBs were cut out at the sample edge in order to facilitate the FIB cutting. During the FIB process, the top surface should indeed be polished from two sides in order to ensure that it is perpendicular to the upper surface. Only in that case is it a pure compression test. If not, there are

some bending stresses. In the present study, it was crucial to have a pure compression in order to get accurate loading stresses, which were used in the simulations. Finally, the pre-prepared sample was cut into a micro-pillar by FIB with FEI Versa 3D Dual Beam system (Hillsboro, OR, USA) using ion beam currents of 15 nA for rough cutting and 1 nA at 30 kV for fine polishing as shown in Figure 1b,d for Ni and α-Brass, respectively. In the present paper, the grain at the edge side of the macrosample is named crystal I and the other one is named crystal II. For the Ni sample, the average length of the micro-pillar was about 15.46 µm and the average width was about 8.03 µm with 4.30 µm for crystal I and 3.73 µm for crystal II. While for the α-Brass sample, the average length of the micro-pillar was about 15.37 µm and the average width was about 9.02 µm with 3.97 µm for crystal I and 5.05 µm for crystal II. Then, the orientations of the bi-crystal were acquired again by EBSD with a spatial step resolution of 0.1 µm. Data processing was performed by AZtec software (2.0, Oxford Instruments, Abingdon, UK) with an indexing rate greater than 99%. The microstructures of the micro-pillars are presented by IPF in Figure 1a for Ni and in Figure 1c for α-Brass. Meanwhile, the slip analysis configuration is presented in Figure 1e. The inclination angle of GB are $\varepsilon = 0°$ for the Ni micro-pillar and $\varepsilon = 6.4°$ for the α-Brass micro-pillar (see Figure 1e).

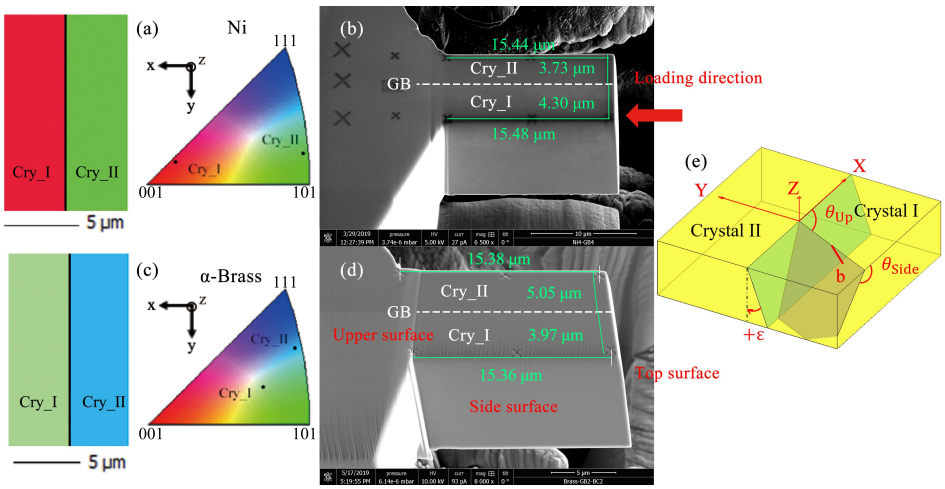

Figure 1. The crystallographic orientations of both crystals, Cry_I and Cry_II, are given in the standard IPF in the direction of the y-axis which is parallel to GB and is also the loading direction of the compression test for (**a**) Ni micro-pillar and (**c**) α-Brass micro-pillar. SEM micrograph of a micro-pillar containing GB cut by FIB for (**b**) Ni sample and (**d**) α-Brass sample; (**e**) schematic figure of slip line analyses: The sample coordinates are set as y perpendicular to GB line on the upper surface pointing towards crystal II, z perpendicular to the upper surface and $x = y \times z$ parallel to the GB line. The angle between the slip line and the GB line in a positive x-direction on the upper surface is noted as θ_{Up}. The angle between the slip line and the upper edge of sample in a positive x-direction on the side surface is noted as θ_{Side}. The inclination angle of GB is noted as ε.

2.4. Micro-Compression Test in SEM

The in-situ compression tests were carried out in high vacuum at room temperature in a Carl Zeiss ΣIGMA series SEM, by an in-situ nanoindenter (UNAT-SEM II) which had a load noise floor level at about 0.002 mN. The micro-pillars were compressed by a diamond flat punch. Furthermore, in order to control the orientation of the micro-pillar well for a pure compression test, such as the loading direction parallel to GB and the top surface of sample perpendicular to flat punch, an additional rotation stage for the sample holder performing rotations in two dimensions was developed. Because the original sample holder could only rotate in one direction, it was necessary to combine it with a complementary rotation stage with two more degrees of freedom. All the compression tests were carried out in displacement controlled mode with several cycles of loading and unloading with small increment as shown in Figure 2a for Ni and in Figure 2b for α-Brass. The idea of loading and unloading cycles is to have enough time to make an SEM picture of high quality in order to well observe slip lines. Once slip lines were observed or yield stress was reached, the compression test was stopped during

the unloading step in order to prevent from the extra force on the pillar coming from the tip vibration when the test was manually interrupted. The loading force and corresponding displacement were recorded during the mechanical tests, so that the stress–strain curves can be calculated after the tests. Even though the cyclic loadings were performed with small increments, the tests were stopped when the first slip event was activated. The first slip event was identified when slip lines were observed in SEM or when yield stress of the bi-crystal was reached. Thus, only the last cycle (marked as red line in Figures 2a,b) contributed to plastic deformation, and all the previous cycles were in the elastic state.

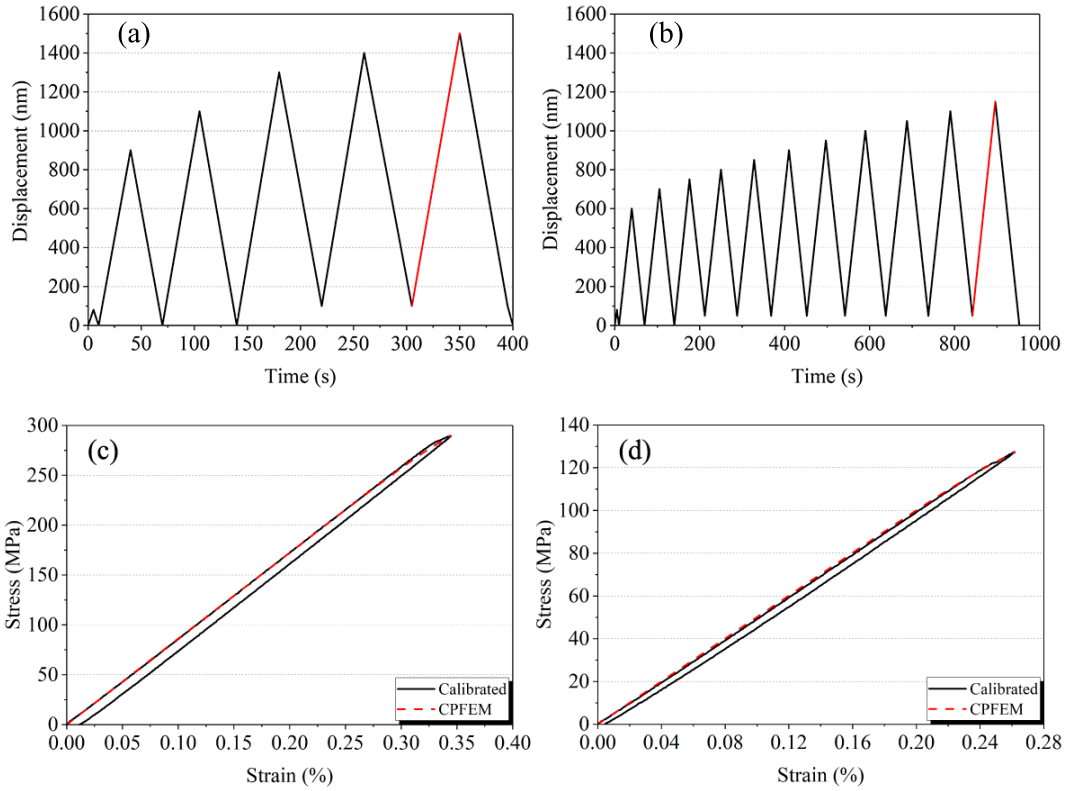

Figure 2. Loading curves obtained with displacement control mode for the compression tests of (**a**) Ni and (**b**) α-Brass. Only red lines contribute to plastic deformation, and all the previous cycles are in the elastic state. Stress–strain curves were corrected by CPFEM simulations for (**c**) the Ni micro-pillar and (**d**) the α-Brass micro-pillar. The applied stress at the end of the compression test is about 289.4 MPa for the Ni sample and 127.4 MPa for the α-Brass sample.

2.5. Stress-Strain Responses and Overall Stresses at Plastic Yielding

Figure 2c,d show the stress–strain responses of the compression tests for Ni and α-Brass, respectively. As designed, most of the deformation was in the elastic state, and only the last small part corresponded to plasticity. However, the yield point occurred at about 8.5% strain for Ni and 6.3% for α-Brass from the originally experimental measurement. These strains are of course too large for characterizing the yield point of such metals. This error came from the drift of the tip during the compression test. Hence, the displacement measurement was not accurate, but the force measurement was accurate. Therefore, CPFEM simulations of the compression tests with the same configuration were performed for both Ni and α-Brass samples. Then, the experimentally measured stress–strain curves were corrected by using CPFEM simulations such that both elastic parts match together. After the correction, the yield point occurred at the stain about 0.33% for Ni and 0.24% for α-Brass, which are reasonable values for such metals. Thus, the effective average loading strain rate was about $7.7 \times 10^{-5}s^{-1}$ for Ni and $5.0 \times 10^{-5}s^{-1}$ for α-Brass. The applied stress at the end of the compression test was about 289.4 MPa for Ni and 127.4 MPa for α-Brass. These values will be used in Section 4.

3. Experimental Results

3.1. Preliminary Slip Analysis Using Schmid Factors and Incompatibility Stresses

Based on the local crystalline orientation, the mechanical and geometrical information of each slip system in the studied grains were firstly analyzed. The slip analysis results for Ni sample and α-Brass sample are reported in Tables 1 and 2, respectively. The results include the Schmid factors, the resolved shear stresses normalized by the applied stress considering elastic incompatibility stresses as detailed in [37,38], the angles between the slip line and the GB line on the upper surface θ_{Up}, the angles between the slip line and the upper edge of sample on the side surface θ_{Side} (see Figure 1e) and the maximum transmission factor with corresponding slip system in the adjacent grain. Here, slip systems in FCC crystals are indicated by Schmid and Boas's notation [39]. The analysis of Schmid factors and resolved shear stresses can be used to predict the first active slip systems (with the maximum Schmid factor or the maximum resolved shear stress) during compressive loading. Schmid factor are computed directly from the projection of the homogeneous external applied stress. However, for the analysis of the resolved shear stresses considering incompatibility stresses, the stresses in the two crystals are the sum of the external applied stress and incompatibility stresses due to heterogeneous elasticity coming from misorientation and anisotropic elasticity [37,38,40]. In some cases, the first active slip system with maximum Schmid factor can be different from the one obtained when considering incompatibility stresses [38,40]. After the mechanical tests, the activated slip lines could be observed by SEM (see Figure 3a for Ni and Figure 4a for α-Brass) and by AFM (see Figure 5a for Ni and Figure 6a for α-Brass). Then, both angles θ_{Up} and θ_{Side} were experimentally determined as shown in Figure 3a (right) for Ni and in Figure 4a (right) for α-Brass. By comparing these angles to the theoretical analyses as described in Tables 1 and 2 (see also Figure 3b for Ni and Figure 4b for α-Brass), the active slip planes were identified. For the present experiments, the onset of plasticity occurred in crystal II for the Ni sample and in crystal I for the α-Brass sample. In both grains, the first active slip system is always the same, either considering a simple Schmid analysis or elastic incompatibility stresses [37,38,40], as marked in red in Tables 1 and 2. However, for the α-Brass sample, combining the analyses provided by Schmid factor and incompatibility stresses, a second slip system could be active as well and is marked in blue in Table 2.

Table 1. Slip system analyses for Ni micro-pillar. The first active slip system is marked in red. The compressive direction is along X, the GB normal along Y and the upper face normal along Z as presented in Figure 1e.

Slip Systesm	Ni Crystal I					Ni Crystal II				
	Schmid Factor	RSS/IS*1	θ_{Up} (°)	θ_{Side} (°)	MTF/CSS*2	Schmid Factor	RSS/IS*1	θ_{Up} (°)	θ_{Side} (°)	MTF/CSS*2
A2	0.0910	0.0246			0.8129/C5	0.0536	0.1087			0.7108/A2
A3	0.3500	0.2960	132.16	40.98	0.8919/C3	0.0373	0.0051	6.11	10.27	0.8250/A3
A6	0.4410	0.3205			0.7393/C1	0.0909	0.1138			0.7049/A6
B2	0.0929	0.1054			0.8635/B5	0.4263	0.5068			0.8984/D4
B4	0.4461	0.3624	58.87	142.12	0.8892/B2	**0.4377**	**0.5270**	**95.09**	**133.01**	**0.8435/B5**
B5	0.3532	0.2570			0.8435/B4	0.0113	0.0202			0.8635/B2
C1	0.0051	0.0419			0.9179/C1	0.3468	0.4131			0.9179/C1
C3	0.4355	0.3354	49.30	61.63	0.9594/C3	0.3606	0.4269	88.56	62.62	0.9594/C3
C5	0.4304	0.2935			0.7803/C5	0.0138	0.0137			0.8129/A2
D1	0.0032	0.0390			0.7801/B4	0.0259	0.0151			0.6515/A6
D4	0.3394	0.2689	150.26	137.01	0.8984/B2	0.0398	0.0950	175.07	5.97	0.6161/B5
D6	0.3394	0.2689			0.8984/B2	0.0658	0.0799			0.6715/A6

∗1 RSS: Resolved shear stress normalized by the applied stress when considering elastic incompatibility stresses (IS) following the formula reported by Richeton and Berbenni [37,38,40]. ∗2 MTF: Maximum transmission factor based on the formula given by Shen et al. [4] with corresponding slip system (CSS) [39] in the adjacent grain.

Table 2. Slip system analyses for α-Brass micro-pillar. The first active slip system is marked in red and the second one in blue. The compressive direction is along X, the GB normal along Y and the upper face normal along Z as presented in Figure 1e.

Slip System	α-Brass Crystal I					α-Brass Crystal II				
	Schmid Factor	RSS/IS	θ_{Up} (°)	θ_{Side} (°)	MTF/CSS	Schmid Factor	RSS/IS	θ_{Up} (°)	θ_{Side} (°)	MTF/CSS
A2	0.2339	0.2075			0.7850/B5	0.1578	0.3233			0.9326/D6
A3	0.2010	0.1073	**115.22**	**109.00**	0.7433/C1	0.0460	0.0431	20.11	15.87	0.9214/D1
A6	**0.4349**	**0.3148**			**0.7750/B2**	0.2038	0.2802			0.9351/D4
B2	0.0305	0.0522			0.7253/B5	0.3944	0.3717			0.7750/A6
B4	0.1086	0.0218	16.08	7.04	0.9287/A6	0.3992	0.3585	64.19	145.40	0.6673/A3
B5	0.0781	0.0740			0.7785/D4	0.0048	0.0132			0.7850/A2
C1	0.3262	0.3366			0.9197/C3	0.1954	0.0783			0.8949/C3
C3	0.1650	0.0084	**45.20**	**91.97**	0.8949/C1	0.2040	0.1278	94.97	77.13	0.9197/C1
C5	**0.4913**	**0.3450**			**0.7182/C5**	0.0085	0.0495			0.7833/A2
D1	0.1228	0.1813			0.9214/A3	0.0412	0.0299			0.7006/D1
D4	0.2573	0.1376	159.65	22.64	0.9417/D6	0.1492	0.2738	167.81	39.88	0.7785/B5
D6	0.1345	0.0437			0.9326/A2	0.1904	0.2439			0.9417/D4

3.2. Slip Analysis by SEM

After the in-situ compression test, the slip lines were firstly analyzed by SEM. Figures 3a and 4a show the observed slip lines in SEM for Ni and α-Brass, respectively. For Ni, the slip lines were very weak on the upper surface and there were only two obvious parallel slip lines for each crystal. Based on the direction of slip lines on the upper surface, the active slip planes were identified as B planes for each crystal as shown in Figure 3. Moreover, the active incoming slip system in the crystal II was identified to be B4 as shown in Figure 3 since it corresponds to the slip system with the highest Schmid factor or the highest RSS given by incompatibility stress formula [37] (see Table 1). Slip system B4 was then considered in the discrete dislocation pile-up simulations (see Section 4). However, for α-Brass, there were two obvious slip lines intersecting the upper surface for crystal I and two obvious slip lines intersecting the side surface for crystal II. Therefore, multiple active slip systems were present in both grains for the α-Brass sample. Based on the analysis of the slip line directions, the active slip planes were determined as A and C for crystal I and B and D for crystal II as shown in Figure 4. Moreover, from the analysis of Schmid factor or incompatibility stresses as described in Table 2, the active incoming slip systems were identified as A6 and C5 for crystal I. Slip system A6 was then considered in the discrete dislocation pile-up simulations due the specific direction of the studied pile-up (see Figure 6).

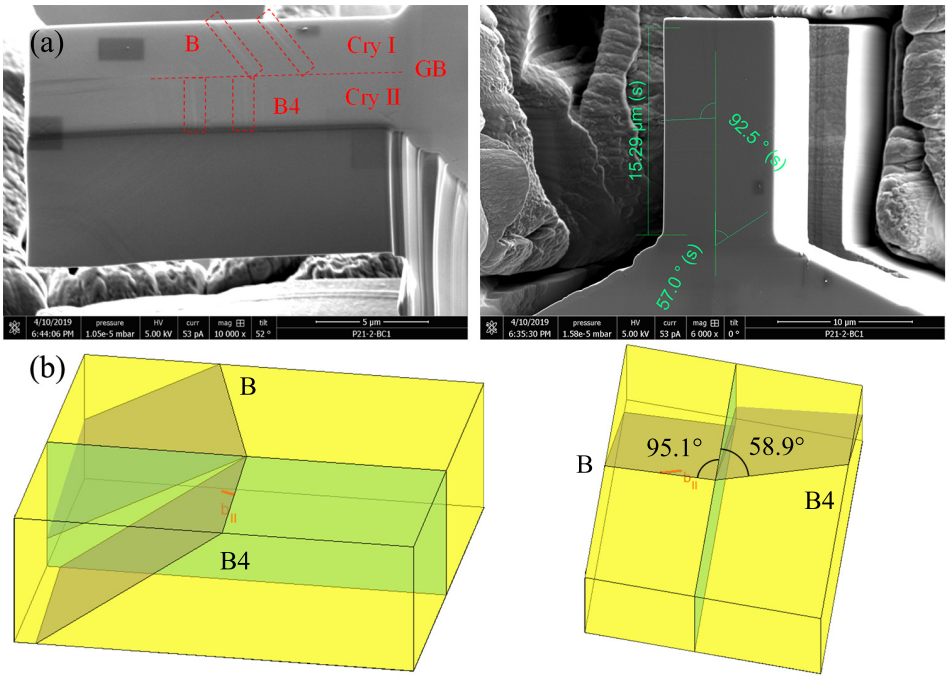

Figure 3. (**a**) crystallographic analysis of slip lines from SEM picture for the Ni sample; (**b**) theoretical analysis of slip systems based on microstructural data (see Table 1).

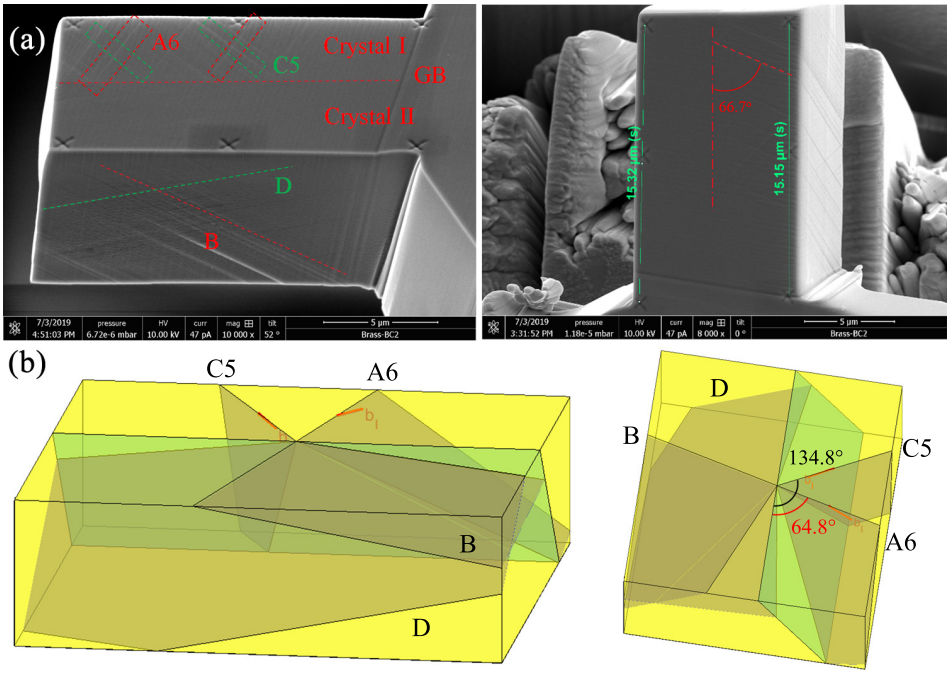

Figure 4. (**a**) crystallographic analysis of slip lines from SEM picture for the α-Brass sample; (**b**) theoretical analysis of slip systems based on microstructural data (see Table 2).

3.3. Slip Analysis by Ex-Situ AFM

AFM measurements were performed on the upper surface by Dimension FastScan with ScanAsyst (Bruker, (Billerica, Mass., USA)) with tapping mode, so that the 3D topography of slip lines can be obtained and used to analyze dislocation distributions. It should be pointed out that these AFM measurements were carried out post-mortem after unloading (ex-situ measurements). The step size of scan was 30 nm with a scan rate of 1 Hz. The results were analyzed by NanoScope Analysis (v180r2sr3, Bruker, Billerica, Mass., USA). They were first of all flattened by polynomial fit of the second order,

and then they were treated by a median filter with 9 × 9 matrix operation. Figures 5a and 6a show the 3D topography of the upper surface of Ni and α-Brass samples, respectively. The slip steps correspond to the slip lines presented in the SEM picture (Figure 3a for Ni and 4a for α-Brass). For the Ni sample, a slip step with classic features of dislocation pile-up was selected for analysis. The heights of the top line and the bottom line of this step were measured along the slip direction from GB which are marked as red and black lines, respectively, in Figure 5a. The measured data are presented in Figure 5c with the corresponding name "Top line" and "Bottom line". Then, they were fitted by the polynomial method which are marked as "Fit h^{Top}" and "Fit h^{Bottom}" in Figure 5c. The relative height of this slip step Δh was calculated as the difference of the fitted heights between these two lines as shown in Figure 5c with the blue line. It was found that the height difference between the two lines at GB, $\Delta h^{\mathrm{GB}} \approx 0.86$ nm, was not zero, which is due to a weak slip transmission and/or dislocation absorption as observed in Figure 5a. The slip step height increased from GB along the slip direction and reached its maximum value $\Delta h \approx 9.06$ nm at about $d \approx 3.28$ µm.

A similar analysis was performed in the crystal I of the α-Brass sample as shown in Figure 6. The observed pile-up had a typical dislocation configuration corresponding to slip on system A6. The slip transmission and/or dislocation absorption were even more intense compared to the Ni sample as $\Delta h^{\mathrm{GB}} \approx 4.29$ nm, but the propagation of dislocations in the adjoining grain had a shorter distance. The maximum of slip step height was $\Delta h \approx 10.03$ nm at about $d \approx 2.44$ µm. There was an obvious peak valley in the middle part of the curve of slip step height, which might be caused by the intersection with another non coplanar slip line.

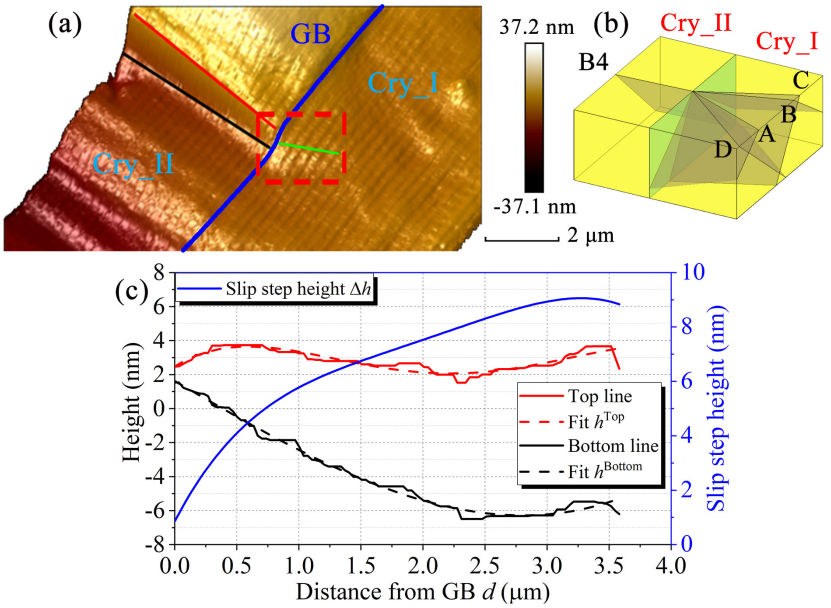

Figure 5. (**a**) ex-situ AFM topographic measurement for the Ni sample. The transmission phenomenon and/or dislocation absorption at GB are surrounded by the frame with red dashed lines. The green line indicates the direction of slip transmission. By comparison of this direction with the schematic presentation of the four slip planes in the crystal I (**b**) and by analysis of the transmission factors in Table 1 (B5 has the largest transmission factor), it can be assumed that the transmission phenomenon occurs in the B slip plane; (**c**) the result of slip step height measurement: red and black solid lines indicate the measured height of the top line and the bottom line of the step, respectively. The dash lines with corresponding color indicate the fitted results by the polynomial method with the correlation coefficient $R^2 = 0.8176$ for the top line and $R^2 = 0.9898$ for the bottom line. The blue line indicates the relative height of the slip step calculated as the difference of the fitted heights.

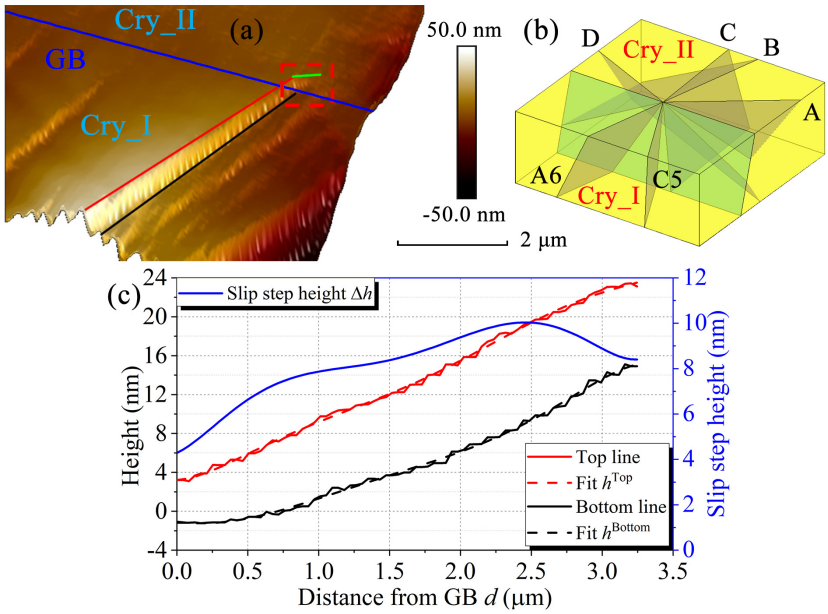

Figure 6. (**a**) ex-situ AFM topographic measurement for the α-Brass sample. The transmission phenomenon and/or dislocation absorption at GB are surrounded by the frame with red dashed lines. The green line indicates the direction of slip transmission. By comparison of this direction with the schematic presentation of the four slip planes in the crystal II (**b**), it can be assumed that the transmission phenomenon occurs in the A slip plane; (**c**) the result of slip step height measurement: red and black solid lines indicate the measured height of the top line and the bottom line of the step, respectively. The dash lines with corresponding color indicate the fitted results by the polynomial method with the correlation coefficient $R^2 = 0.9982$ for the top line and $R^2 = 0.9973$ for the bottom line. The blue line indicates the relative height of the slip step calculated as the difference of the fitted heights.

4. Discrete Dislocation Pile-Up Simulations and Discussion

4.1. Discrete Dislocation Pile-Up Configuration in Heterogeneous and Anisotropic Elasticity

First of all, let us consider the single slip configuration of a single dislocation-ended discrete pile-up in a bi-crystal model accounting for heterogeneous anisotropic elasticity. There are N infinite straight dislocations in the pile-up, which are all parallel to the $\boldsymbol{x}_3$-axis, having the same Burgers vector $\boldsymbol{b}$ and lying in the same slip plane as shown in Figure 7a.

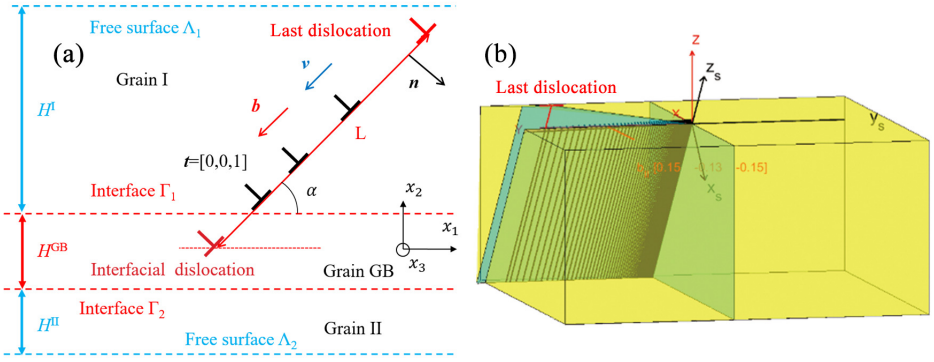

Figure 7. (**a**) α-inclined single-ended discrete dislocation pile-up in a slip plane of unit normal $\boldsymbol{n}$ for N equilibrated edge dislocations with Burgers vector $\boldsymbol{b}$ and line vector $\boldsymbol{t}$ in a heterogeneous anisotropic bi-crystalline micro-pillar. GB is regarded as an interphase of thickness H^{GB} bounded by two planar interfaces Γ_1 and Γ_2. If the free surfaces Λ_1 and Λ_2 are considered, Grain I and Grain II are finite with the corresponding thickness H^{I} and H^{II}. Conversely, when free surfaces are not considered, Grain I and Grain II are infinite, thus there are only two interfaces Γ_1 and Γ_2 and the free surfaces Λ_1 and Λ_2 do not exist; (**b**) schematic figure of the simulation configuration adopted for the experiment. (x_S, y_S, z_S) indicate the simulation coordinates system, while (X, Y, Z) indicates the global sample coordinates system.

The equilibrium positions of the N dislocations can be found out by minimizing the component of the Peach–Koehler (P–K) force along the slip direction for each dislocation to a material's critical force F_c as follows:

$$F^{(\gamma)} = \text{abs}(\{(\boldsymbol{\sigma}_{\text{int}}(X_1(\gamma), X_2(\gamma)) + \boldsymbol{\sigma}_{\text{ext}}) \cdot \boldsymbol{b} \times \boldsymbol{t}\} \cdot \boldsymbol{v}) \overset{\text{Minimize}}{=\!=\!=} F_c \quad (1)$$

where $(X_1(\gamma), X_2(\gamma))$ denotes the position of the γth dislocation. $\boldsymbol{v}$ is a unit vector that belongs to the slip plane and is normal to the dislocation line. It indicates the glide direction of all the dislocations. It is considered to be directed towards the GB so that a pile-up can form. $\boldsymbol{\sigma}_{\text{ext}}$ is a homogeneous applied stress tensor to the bi-crystal and $\boldsymbol{\sigma}_{\text{int}} = \boldsymbol{\sigma}_{\text{im}} + \boldsymbol{\sigma}_{\text{dis}}$ is the internal stress tensor produced by all the other dislocations, $\boldsymbol{\sigma}_{\text{dis}}$, and the image stress tensor $\boldsymbol{\sigma}_{\text{im}}$ on this particular dislocation coming from all elastic heterogeneities, see the detailed calculations in [41] using the Leknitskii–Eshelby–Stroh (L–E–S) formalism for two-dimensional anisotropic elasticity. Here, the elastic heterogeneities include the GB seen as an interphase [41], both grains related by a misorientation and two free surfaces (denoted as Λ_1 and Λ_2 in Figure 7a). The interphase is supposed to be the region between two planar interfaces Γ_1 and Γ_2 with a thickness H^{GB} as shown in Figure 7a. The image stress produced by these heterogeneities can be calculated using the image decomposition method for anisotropic multilayers [42]. In this method, all the interfaces and the free surfaces are regarded as a distribution of image dislocation densities which can be resolved through boundary conditions [42]. The interphase model allows considering a non-zero thickness in the nanometer range and a specific elastic stiffness tensor for the GB region. While the configuration with two free surfaces can be used to study size effects [43], more discussions about the interphase model and the effect of free surfaces can be found in [44]. At the end, the critical force F_c may include the lattice friction force (primary) and other forces due to obstacles to dislocation motion (solute atoms, precipitates, etc.). Meanwhile, this critical force can be converted into a shear stress on a dislocation by dividing by the corresponding Burgers vector magnitude as $\tau_c = F_c / |\boldsymbol{b}|$. Most past studies assume $F_c = 0$ N/m in Equation (1) because of the low value of the lattice friction stress in pure FCC crystals, which is around $1 \sim 2$ MPa [45]. However, in the present study, it is found that a non-zero critical force has a crucial effect on the discrete distribution of dislocations in the presence of GB and free surfaces. The reason is that there are already lattice defects in the material after sample preparation, such as the Ga^+ ions from FIB [46]. Furthermore, for α-Brass, the theoretical value of the lattice friction force should be higher than in pure FCC crystals, like pure Ni. Thus, the critical force cannot be ignored in Equation (1) for realistic discrete pile-up calculations. The calculations of the discrete dislocation pile-up equilibrium positions are thus obtained by following an iterative relaxation scheme that minimizes all the $F^{(\gamma)}$ after an initial configuration is specified [41,47].

4.2. Simulation Configuration of Experiments

Combined with the discussion of image stress effects [41,44], the slip step heights due to a dislocation pile-up measured in experiments (see Figure 5c for Ni and Figure 6c for α-Brass) can be simulated in a bi-crystal configuration containing a GB and two free surfaces using a discrete dislocation pile-up modelling in heterogeneous anisotropic elasticity. The hypotheses and configurations are set as follows and presented in Figure 7:

1. The dislocation lines are supposed to be infinite straight lines. They are parallel to each other and also parallel to the GB plane.
2. For the simulation coordinates system, the $\boldsymbol{x_3}$ direction is set to be the direction of dislocation line z_S, and the $\boldsymbol{x_2}$ direction is set to be the direction of GB normal y_S as presented in Figure 7b. Then, $\boldsymbol{x_1}$ is determined by the vector product $\boldsymbol{x_1} = \boldsymbol{x_2} \times \boldsymbol{x_3}$ which is presented as x_S in Figure 7b. Furthermore, all the used vectors and tensors, such as the Burgers vector of active slip system, the slip direction vector, and the elastic stiffness tensor, etc. are transformed into the simulation coordinates system.

3. The position of the maximum slip step height measured in the experiment is considered to be the end of the discrete dislocation pile-up. However, in the model, the last dislocation is fixed at the position of the observed maximum slip step height. Hence, the length of the dislocation pile-up as shown in Figure 7 is the same in all the simulations. The P–K force on this last dislocation is not zero. It is assumed that this dislocation is locked on some material defect not considered in the simulation. Furthermore, it is supposed that there is no more dislocation between the maximum slip step height and the side free surface as if the dislocations in this area have escaped through the side free surface.
4. All the presented simulations are performed by the image decomposition method for anisotropic multilayers problem which only considers linear anisotropic elasticity [42,44]. In the present study, a three layers configuration is used. GB is always regarded as an elastic interphase with a thickness $H^{\mathrm{GB}} = 0.9$ nm (the second layer in the model, marked as Grain GB in Figure 7a). This value has been obtained from Molecular Statics (MS) simulations on the Ni sample. The stiffness tensor of this interphase is here simply modeled as a first approximation by $C^{\mathrm{GB}}_{ijkl} = \left(C^{\mathrm{I}}_{ijkl} + C^{\mathrm{II}}_{ijkl}\right)/2$, which is the average of the two grains' elastic stiffness tensors.
5. As the theory is two-dimensional (invariance along the dislocation line), dislocations with different line directions cannot be considered at the same time. Thus, the transmitted and/or absorbed dislocations are modeled as an interfacial super-dislocation fixed in the middle of the GB interphase. Therefore, $\boldsymbol{b}^{\mathrm{Tran}} = N^{\mathrm{Tran}} \times \boldsymbol{b}^{\mathrm{GB}}$, where $\boldsymbol{b}^{\mathrm{Tran}}$ is the Burgers vector of the super-dislocation, N^{Tran} the number of transmitted and/or absorbed dislocations, and $\boldsymbol{b}^{\mathrm{GB}}$ is the Burgers vector of dislocations stored at GB. $\boldsymbol{b}^{\mathrm{GB}}$ can be equal to the Burgers vector of the incoming dislocations, or equal to the residual Burgers vector between incoming slip system ($\boldsymbol{b}^{\mathrm{In}}$) and one of the 12 outgoing slip systems ($\boldsymbol{b}^{\mathrm{Out}}$) in the adjacent grain defined as $\boldsymbol{b}^{\mathrm{GB}} = \boldsymbol{b}^{\mathrm{In}} - \boldsymbol{b}^{\mathrm{Out}}$.
6. For the present results, the applied stress tensor $\boldsymbol{\sigma}_{\mathrm{ext}}$ is always considered as homogeneous in both grains without considering incompatibility stresses [37,38,40,41]. Thus, $\boldsymbol{\sigma}_{\mathrm{ext}}$ has only one non-zero component σ_X in the global sample coordinate system (see Figure 7b), which is considered as a uniaxial compression test along the GB direction. The value of σ_X for each sample is the maximum applied stress in the compression test, which can be obtained from experimental stress–strain curves, thus $\sigma_X = 289.4$ MPa for the Ni sample and $\sigma_X = 127.4$ MPa for the α-Brass sample (see Figure 2c,d).
7. If not specifically stated in the text, the default value of the critical force is equal to zero, as $F_c = 0$ N/m. This default value will only correspond to Simulations 1 and 2 in Section 4.3.
8. The equilibrium positions of the dislocations in the pile-up are determined by Equation (1), then the slip step height at a given position along the slip direction can be calculated by:

$$\Delta h(d) = N(d) \times b(\mathrm{Z}) \tag{2}$$

   where d is the distance from GB along slip direction, N the number of dislocations in the dislocation pile-up from GB to the position d, and $b(\mathrm{Z})$ is the out-of-surface component of the Burgers vector (along Z direction, which is perpendicular to the upper surface as shown in Figure 7b).
9. In the following parts, the measured slip step height is calibrated to be zero at GB, which means $\Delta h = h^{\mathrm{Top}} - h^{\mathrm{Bottom}} - \Delta h^{\mathrm{GB}}$. Similarly, the simulated slip step height profile is considered to be zero at GB as $\Delta h(0) = 0$.

4.3. Simulation Results and Discussions

4.3.1. Results for Ni Sample

Based on the hypotheses described in Section 4.2 and considering the B4 slip system in the crystal II of the studied Ni sample, the out-of-surface component of the Burgers vector is about 0.15 nm. The maximum slip step height is about 9.1 nm at $d \approx 3.28$ µm and the slip step height at GB due to slip transmission and/or dislocation absorption is about 0.86 nm. Thus, based on Equation (2), the number of dislocations in the pile-up is 61 and the number of transmitted and/or absorbed dislocations is 6. Therefore, the number of dislocations in the pile-up is equal to 55. The applied stress is 289.4 MPa as measured in experiment, and it corresponds to a resolved shear stress $\tau = 129.0$ MPa. The thicknesses of Grains I and II are $H^{\mathrm{I}} = 4.30$ µm and $H^{\mathrm{II}} = 3.73$ µm as shown in Figure 1b. With all these parameters, the slip step height distribution due to dislocations in the pile-up was simulated for different critical forces while considering or not the effect of free surfaces as shown in Figure 8a.

Comparing the result of Simulation 1 without free surfaces to Simulation 2 with two free surfaces, it is found that the free surfaces have an influence on dislocations behavior. From the theory, it is known that free surfaces have always an attractive effect on dislocations. When the dislocations are closer to the first free surface Λ_1 than the second one Λ_2 (see Figure 7a), the total force without considering the stress field of the last dislocation is always towards Λ_1, and so dislocations move towards the last dislocation to reach equilibrium. However, the dislocations around GB are nearly in the middle of both free surfaces, thus the effects of the two free surfaces are balanced out by each other. Therefore, the free surfaces have much more effects on the dislocations which are near the free surface rather than the ones which are located around GB. These two simulation results are close to the experimental measurement, but there are still some discrepancies. Compared to the experimental measurement, the dislocations are closer to GB without free surfaces, while they are closer to the first free surface when considering the effect of free surfaces.

As discussed in Section 4.1, it is actually necessary to consider the effect of critical force F_c (see Equation (1)). After the analysis of the results with different value of F_c, it is found that F_c moves the dislocations towards the GB. When considering the effect of free surfaces with a material's critical force $F_c = 0.003$ N/m in Equation (1) (equivalent to a resolved shear stress $\tau_c = 12$ MPa), the simulation result is closer to the experimental measurement as shown in Figure 8a with Simulation 3. Here, the value is higher than the theoretical value of lattice friction for pure FCC crystals which is around $1 \sim 2$ MPa [45]. The reason might be due to the sample preparation, such as defects coming from FIB polishing. Furthermore, as discussed in Section 4.2 (3), the P–K force is not zero on the last fixed dislocation. The total resolved shear stresses on this fixed dislocation are 6.6 MPa for Simulation 1, 175.0 MPa for Simulation 2 and 71.2 MPa for Simulation 3. The value found in Simulation 2 is quite high for a FCC crystal and appears unrealistic.

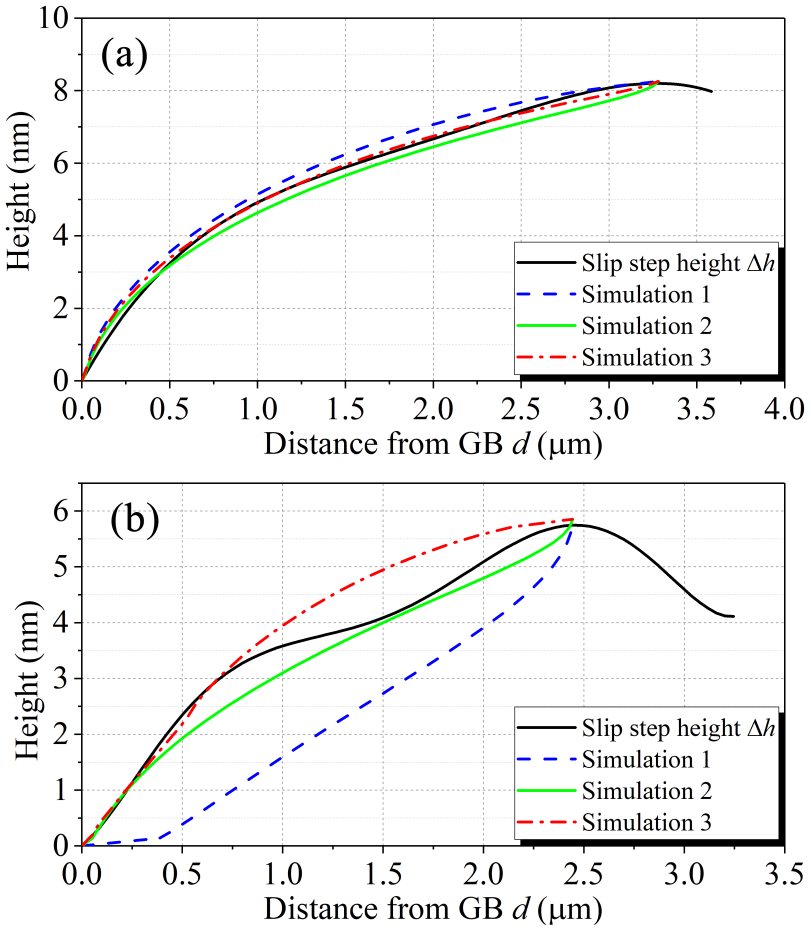

Figure 8. (**a**) simulation of slip step height profile for Ni with different discrete dislocation pile-up simulation conditions ($\boldsymbol{b}^{\mathrm{GB}}$ is always the same as $\boldsymbol{b}^{\mathrm{In}}$). Simulation 1: without free surfaces. Simulation 2: with two free surfaces. Simulation 3: with two free surfaces and a non zero material dependent critical force $F_c = 0.003$ N/m; (**b**) simulation of slip step height profile for α-Brass with different discrete dislocation pile-up simulation conditions (always with two free surfaces). Simulation 1: $\boldsymbol{b}^{\mathrm{GB}} = \boldsymbol{b}^{\mathrm{In}}$. Simulation 2: $\boldsymbol{b}^{\mathrm{GB}} = \boldsymbol{b}^{\mathrm{In}} - \boldsymbol{b}^{\mathrm{Out}}$ (A6). Simulation 3: $\boldsymbol{b}^{\mathrm{GB}} = \boldsymbol{b}^{\mathrm{In}} - \boldsymbol{b}^{\mathrm{Out}}$ (A6) with a non zero material dependent critical force $F_c = 0.011$ N/m.

4.3.2. Results for the α-Brass Sample

Similarly to the Ni sample, the same simulations have been performed for the A6 slip system in the crystal I of the α-Brass sample. In this case, the out-of-surface component of the Burgers vector is about 0.14 nm. The maximum slip step height is about 10.03 nm at $d \approx 2.44$ μm and the slip step height at GB due to slip transmission and/or dislocation absorption is about 4.29 nm. Based on Equation (2), the number of dislocations in the pile-up is 72 and the number of transmitted and/or absorbed dislocations is 31. Therefore, the number of dislocations in the pile-up is equal to 41. The applied stress is 127.4 MPa following experimental results, and it corresponds to a resolved shear stress $\tau = 55.4$ MPa. The thicknesses of Grains I and II are $H^{\mathrm{I}} = 3.97$ μm and $H^{\mathrm{II}} = 5.05$ μm as shown in Figure 1d.

The effects of free surfaces and critical force for the α-Brass sample are the same as for the Ni sample. However, the number of transmitted and/or absorbed dislocations is much larger in the α-Brass sample than in the Ni one, i.e., 31 instead of 6. Thus, the repulsive force from these interfacial dislocations is more important if their Burgers vector is considered as the same as the incoming dislocations (see the Simulation 1 in Figure 8b). All dislocations are moved far away from GB into the direction of free surface due to this repulsive force. The transmission mechanism observed in Figure 6a leads us to consider a different residual Burgers vector for interfacial dislocations. After verifying all the possible residual Burgers vectors with the 12 slip systems in the adjacent grain, it is found that the best solution is with A6 slip system in the adjacent grain while considering free surfaces and

a reasonable critical force $F_c = 0.011$ N/m ($\tau_c = 43$ MPa) as shown in Figure 8b with Simulation 3. Furthermore, the theoretical analysis of the slip trace of A6 slip system on the upper surface of the adjacent grain agrees well with the experimental observation as shown in Figure 6a compared to other slip systems, such as B2 slip system with the maximum transmission factor [4] or B4 slip system with the maximum Schmid factor in the adjacent grain (see Table 2). As discussed in Section 3.3 for the α-Brass sample, the peak valley in the middle part of the measured curve is certainly caused by the crossing with a second non coplanar active slip system. In the present L–E–S two-dimensional anisotropic elastic theory, it is not possible to consider the effect of two dislocations whose dislocation lines are not parallel. Thus, this effect of peak valley part cannot be simulated within the present theory. However, it is important to well identify the part close to GB with $d < 0.75$ µm. Here, the suitable critical stress is $\tau_c = 43$ MPa. It is larger than the critical stress for the Ni sample, which may be due to alloying element hardening. Furthermore, the total resolved shear stresses for the last fixed dislocation are 997.3 MPa for Simulation 1, 258.9 MPa for Simulation 2 and 28.6 MPa for Simulation 3. Thus, Simulation 3 appears to be the most realistic one.

4.3.3. Discussion

Except the free surfaces effects, it is found that the Burgers vector of interfacial dislocations has an obvious influence on the dislocation distribution in the pile-up. It should be pointed out that, for the Ni sample, $\boldsymbol{b}^{\mathrm{GB}}$ has been tried with all the 12 residual Burgers vectors, but the results are never better than in the case with $\boldsymbol{b}^{\mathrm{GB}} = \boldsymbol{b}^{\mathrm{In}}$. Thus, the Burgers vector of interfacial dislocations can be regarded as the same as incoming dislocations in case of a low number (6) of transmitted and/or absorbed dislocations in the Ni sample. However, in case of a high number (31) of transmitted and/or absorbed dislocations in the α-Brass sample, one needs to consider the residual Burgers vector of interfacial dislocations.

In addition to the effects of interfacial dislocations, the critical force is also another important parameter to find the correct equilibrated dislocation distribution. Comparing the simulation 2 ($F_c = 0$ N/m) with the Simulation 3 ($F_c \neq 0$ N/m) presented in Figure 8 for both Ni and α-Brass samples, it is found that the critical force does not have an obvious effect on dislocations that are located at a distance less than 0.3 µm from GB. From Equation (1), it is found that this critical force does not have a uniform effect on all the dislocations within the pile-up. For example, when the total force on a dislocation is towards free surface for positions close to the free surface, the critical force will point towards the GB. However, the stress state is more complicated in regions close to the GB. The total force on a dislocation here can point towards the GB due to repulsive forces from other dislocations, attractive misorientation [41], compliant GB [41], attractive force from interfacial dislocations, and applied stress. On the contrary, it can point towards the opposite direction due to repulsive misorientation [41], rigid GB [41], repulsive force from interfacial dislocations, other dislocations, and free surfaces. Hence, the total force depends on many physical parameters. Thus, the critical force could either move the dislocations towards GB or to the opposite direction.

As mentioned in Section 3.3, the ex-situ AFM measurements were carried out after compression and elastic unloading; thus, for the present static dislocation pile-up simulation, the applied stress should be set to zero. However, in the present study, the dislocations in the pile-up are supposed to be unchanged during unloading, which means that the equilibrium positions of dislocations obtained at the onset of plastic loading are consistent before and after unloading process due to a large critical force in the crystal. The found critical forces $F_c = 0.003$ N/m for Ni and $F_c = 0.011$ N/m for α-Brass are supposed to be the original critical force before slip activation with a low dislocation density in the crystal.

Furthermore, the effects of incompatibility stresses [37], elastic anisotropy compared to elastic isotropy, number of interfacial dislocations, applied stress, and misorientation can be also investigated with the developed model [44]. As a summary, for the present samples, the main effects come from the

external stress, heterogeneous and anisotropic elasticity, and the number of interfacial dislocations which should be equal to the one of the transmitted and/or absorbed dislocations.

In Figure 8b, it was also found that the measured slip step height decreases significantly after its maximum value along the slip direction. This tendency might be the signature of a double-ended dislocation pile-up due to a less penetrable layer than the free surface coming from surface defects produced by FIB polishing. The effect of these surface defects seems to be stronger for the α-Brass sample compared to the Ni sample. Hence, the present model which was designed to account for single slip within a single-ended dislocation pile-up configuration is more suitable for the study of the Ni sample than the α-brass sample. In general, the present model can be applied to any crystalline structure where dislocation pile-ups can be characterized experimentally. However, it is more suitable for FCC materials where slip is relatively planar.

5. Conclusions

In this work, experimental studies of Burgers vector distribution in discrete dislocation pile-ups at GB were performed in Ni and α-Brass bi-crystalline micro-pillars. Ex-situ AFM measurements were carried out after a compression test with a flat punch nanoindenter. The measured slip step heights were simulated using a three anisotropic layers model combined with image stress calculation [42], which was more suitable for a single-ended dislocation pile-up configuration with single slip compared to multi-slip configurations. In this model, GB was regarded as an elastic interphase with a thickness $H^{\mathrm{GB}} = 0.9$ nm, which was obtained from MS simulations. Meanwhile, the effects of two free surfaces around micro-pillars were considered. It was found that, for the Ni sample, the best solution of this simulation was obtained considering anisotropic elasticity, the effect of free surfaces, a critical shear stress $\tau_c = 12$ MPa, a homogeneous external stress, and the same Burgers vector of incoming dislocations and interfacial dislocations. However, for the α-Brass sample, still considering anisotropic elasticity, the best solution was obtained with free surfaces, a homogeneous external stress field, and a larger critical shear stress of $\tau_c = 43$ MPa. In addition, the Burgers vector of interfacial dislocations was modeled as a residual Burgers vector because there was a huge number of transmitted and/or absorbed dislocations.

Author Contributions: Conceptualization, X.C., T.R., C.M., and S.B.; methodology, X.C., T.R., C.M., and S.B.; software, X.C.; validation, T.R., C.M., and S.B.; formal analysis, X.C., T.R., C.M., and S.B.; investigation, X.C.; resources, C.M. and S.B.; data curation, X.C.; writing—original draft preparation, X.C.; writing—review and editing, T.R., C.M., and S.B.; visualization, X.C.; supervision and project administration, S.B.; funding acquisition, C.M. and S.B. All authors have read and agreed to the published version of the manuscript.

Funding: The authors are grateful to the French Ministry of Higher Education and Scientific Research and the French-German University (UFA-DFH) for financial supports. The authors are also grateful to Experimental Methodology in Materials Science (MWW) in Saarland University and the French State (ANR) through the program "Investment in the future" (LabEx "DAMAS" referenced as ANR-11-LABX-0008-01) for additional financial supports. We also would like to thank the Deutsche Forschungsgemeinschaft DFG for the financing of the AFM microscope, Grant No. INST 256/455-1 FUGG.

Acknowledgments: The authors would like to thank J. Rafael Velayarce for his help with the experiments.

Conflicts of Interest: The authors declare no conflict of interest.

Abbreviations

The following abbreviations are used in this manuscript:

GB(s)	Grain Boundary(ies)
FCC	Face-Centered Cubic
Ni	Nickel
AFM	Atomic Force Microscopy
TEM	Transmission Electron Microscope
EBSD	Electron Back Scattered Diffraction
SEM	Scanning Electron Microscope

ECCI	Electron Channelling Contrast Imaging
CPFEM	Crystal Plasticity Finite Element Method
DDD	Discrete Dislocation Dynamics
MD	Molecular Dynamics
MS	Molecular Statics
RSS	Resolved Shear Stress
IS	Incompatibility Stresses
CSS	Corresponding Slip System
P–K	Peach–Koehler
L-E-S	Leknitskii–Eshelby–Stroh

References

1. Hall, E.O. The deformation and ageing of mild steel: III discussion of results. *Proc. Phys. Soc. Sect. B* **1951**, *64*, 747–753. [CrossRef]
2. Petch, N.J. The cleavage strength of polycrystals. *J. Iron Steel Inst.* **1953**, *174*, 25–30.
3. Armstrong, R.W. The influence of polycrystal grain size on several mechanical properties of materials. *Metall. Mater. Trans. B* **1970**, *1*, 1169–1174. [CrossRef]
4. Shen, Z.; Wagoner, R.H.; Clark, W.A.T. Dislocation and grain boundary interactions in metals. *Acta Metall.* **1988**, *36*, 3231–3242. [CrossRef]
5. Kamaya, M.; Wilkinson, A.J.; Titchmarsh, J.M. Measurement of plastic strain of polycrystalline material by electron backscatter diffraction. *Nucl. Eng. Des.* **2005**, *235*, 713–725. [CrossRef]
6. Pantleon, W. Resolving the geometrically necessary dislocation content by conventional electron backscattering diffraction. *Scr. Mater.* **2008**, *58*, 994–997. [CrossRef]
7. Gutierrez-Urrutia, I.; Zaefferer, S.; Raabe, D. Coupling of Electron Channeling with EBSD: Toward the Quantitative Characterization of Deformation Structures in the SEM. *JOM* **2013**, *65*, 1229–1236. [CrossRef]
8. Perrin, C.; Berbenni, S.; Vehoff, H.; Berveiller, M. Role of discrete intra-granular slip on lattice rotations in polycrystalline Ni: Experimental and micromechanical studies. *Acta Mater.* **2010**, *58*, 4639–4649. [CrossRef]
9. Kahloun, C.; Badji, R.; Bacroix, B.; Bouabdallah, M. Contribution to crystallographic slip assessment by means of topographic measurements achieved with Atomic Force Microscopy. *Mater. Charact.* **2010**, *61*, 835–844. [CrossRef]
10. Kahloun, C.; Monnet, G.; Queyreau, S.; Le, L.T.; Franciosi, P. A comparison of collective dislocation motion from single slip quantitative topographic analysis during in-situ AFM room temperature tensile tests on Cu and Feα crystals. *Int. J. Plast.* **2016**, *84*, 277–298. [CrossRef]
11. Dehm, G.; Jaya, B.N.; Raghavan, R.; Kirchlechner, C. Overview on micro-and nanomechanical testing: New insights in interface plasticity and fracture at small length scales. *Acta Mater.* **2018**, *142*, 248–282. [CrossRef]
12. Clark, W.A.T.; Wise, C.E.; Shen, Z.; Wagoner, R.H. The use of the transmission electron-microscope in analyzing slip propagation across interfaces. *Ultramicroscopy* **1989**, *30*, 76–89. [CrossRef]
13. Gleiter, H.; Hornbogen, E.; Ro, G. The mechanism of grain boundary glide. *Acta Metall.* **1968**, *16*, 1053–1067. [CrossRef]
14. Pumphrey, P.H.; Gleiter, H. Annealing of dislocations in high-angle grain boundaries. *Philos. Mag. J. Theor. Exp. Appl. Phys.* **1974**, *30*, 593–602. [CrossRef]
15. Bayerschen, E.; McBride, A.T.; Reddy, B.D.; Böhlke, T. Review on slip transmission criteria in experiments and crystal plasticity models. *J. Mater. Sci.* **2016**, *51*, 2243–2258. [CrossRef]
16. Hunter, A.; Leu, B.; Beyerlein, I.J. A review of slip transfer: applications of mesoscale techniques. *J. Mater. Sci.* **2018**, *53*, 5584–5603. [CrossRef]
17. Livingston, J.D.; Chalmers, B. Difference fatigue cracking behaviors of Cu bicrystals with the same component grains but different twin boundaries. *Acta Metall.* **1957**, *5*, 322–327. [CrossRef]
18. Beyerlein, I.; Mara, N.; Wang, J.; Carpenter, J.; Zheng, S.; Han, W.; Zhang, R.; Kang, K.; Nizolek, T.; Pollock, T. Structure-property-functionality of bimetal interfaces. *JOM* **2012**, *64*, 1192–1207. [CrossRef]
19. Werner, E.; Prantl, W. Slip transfer across grain and phase boundaries. *Acta Metall. Mater.* **1990**, *38*, 533–537. [CrossRef]

20. Head, A.K. X. The Interaction of Dislocations and Boundaries. *Lond. Edinb. Dublin Philos. Mag. J. Sci.* **1953**, *44*, 92–94. [CrossRef]
21. Pacheco, E.S.; Mura, T. Interaction between a screw dislocation and a bimetallic interface. *J. Mech. Phys. Solids* **1969**, *17*, 163–170. [CrossRef]
22. Koehler, J.S. Attempt to Design a Strong Solid. *Phys. Rev. B* **1970**, *2*, 547–551. [CrossRef]
23. Krzanowski, J.E. The effect of composition profile shape on the strength of metallic multilayer structures. *Scr. Metall. Mater.* **1991**, *25*, 1465–1470. [CrossRef]
24. Anderson, P.M.; Xin, X.J. The critical shear stress to transmit a peierls screw dislocation across a non-slipping interface. In *Multiscale Deformation and Fracture in Materials and Structures. Solid Mechanics and Its Applications*; Chuang T.J., Rudnicki J.W., Eds.; Springer Science & Business Media: Berlin, Germany, 2000, Volume 84, pp. 87–105.
25. Imrich, P.J.; Kirchlechner, C.; Motz, C.; Dehm, G. Differences in deformation behavior of bicrystalline Cu micropillars containing a twin boundary or a large-angle grain boundary. *Acta Mater.* **2014**, *73*, 240–250. [CrossRef]
26. Imrich, P.J.; Kirchlechner, C.; Dehm, G. Influence of inclined twin boundaries on the deformation behavior of Cu micropillars. *Mater. Sci. Eng. A* **2015**, *642*, 65–70. [CrossRef]
27. Knorr, A.F.; Marx, M.; Schaefer, F. Crack initiation at twin boundaries due to slip system mismatch. *Scr. Mater.* **2015**, *94*, 48–51. [CrossRef]
28. Malyar, N.V.; Micha, J.-S.; Dehm, G.; Kirchlechner, C. Dislocation-twin boundary interaction in small scale Cu bi-crystals loaded in different crystallographic directions. *Acta Mater.* **2017**, *129*, 91–97. [CrossRef]
29. Kheradmand, N.; Vehoff, H.; Barnoush, A. An insight into the role of the grain boundary in plastic deformation by means of a bicrystalline pillar compression test and atomistic simulation. *Acta Mater.* **2013**, *61*, 7454–7465. [CrossRef]
30. Anderson, P.M.; Hirth, J.P.; Lothe J. *Theory of Dislocations*, 3rd Ed.; Cambridge University Press: Cambridge, UK, 2017.
31. Rayne, J.A. Elastic Constants of α-Brasses: Room-Temperature Variation with Solute Concentration. *Phys. Rev.* **1958**, *112*, 1125–1130. [CrossRef]
32. Rayne, J.A. Elastic Constants of α-Brasses: Variation with Solute Concentration from 4.2–300 °K. *Phys. Rev.* **1959**, *115*, 63–66. [CrossRef]
33. Zhao, Y.H.; Liao, X.Z.; Zhu, Y.T.; Horita, Z.; Langdon, T.G. Influence of stacking fault energy on nanostructure formation under high pressure torsion. *Mater. Sci. Eng. A* **2005**, *410–411*, 188–193. [CrossRef]
34. Rémy, L. Maclage et transformation martensitique CFC $\rightarrow$ HC induite par déformation plastique dans les alliages austénitiques à basse énergie de défaut d'empilement des sytèmes CO-NI-CR-MO et FE-MN-CR-C. Ph.D Thesis, Université de Paris-Sud, Orsay, France, 1975.
35. Tiba, I. Effets des Interfaces Cristallines sur les Champs méCaniques en Plasticité Cristalline et conséQuences sur le Glissement Dans des Micro-Pilliers Bi-Cristallins. Ph.D. Thesis, Université de Lorraine et Université de Saarbrücken, Metz, France, 2015.
36. Itoh, I.; Hikage, T. Dezincification Mechanism of Brass in Vacuum at High Temperature. *Trans. Jpn. Inst. Met.* **1976**, *17*, 165–169. [CrossRef]
37. Richeton, T.; Berbenni, S. Effects of heterogeneous elasticity coupled to plasticity on stresses and lattice rotations in bicrystals: A Field Dislocation Mechanics viewpoint. *Eur. J. Mech. A/Solids* **2013**, *37*, 231–247. [CrossRef]
38. Tiba, I.; Richeton, T.; Motz, C.; Vehoff, H.; Berbenni, S. Incompatibility stresses at grain boundaries in Ni bicrystalline micropillars analyzed by an anisotropic model and slip activity. *Acta Mater.* **2015**, *83*, 227–238. [CrossRef]
39. Schmid, E.; Boas, W. *Kristallplastizität mit Besonderer Berücksichtigung der Metalle*; Springer: New York, NY, USA, 1935.
40. Richeton, T.; Tiba, I.; Berbenni, S.; Bouaziz, O. Analytical expressions of incompatibility stresses at $\Sigma 3\,\langle 111\rangle$ twin boundaries and consequences on single-slip promotion parallel to twin plane. *Philos. Mag.* **2015**, *95*, 12–31. [CrossRef]
41. Chen, X.; Richeton, T.; Motz, C.; Berbenni, S. Elastic fields due to dislocations in anisotropic bi- and tri-materials: Applications to discrete dislocation pile-ups at grain boundaries. *Int. J. Solids Struct.* **2019**, *164*, 141–156. [CrossRef]

42. Wang, H.Y.; Wu, M.S.; Fan, H. Image decomposition method for the analysis of a mixed dislocation in a general multilayer. *Int. J. Solids Struct.* **2007**, *44*, 1563–1581. [CrossRef]
43. Rafael Velayarce, J.; Motz, C. Effect of Sample Size and Crystal Orientation on the Fatigue Behaviour of Single Crystalline Microbeams. *Materials* **2020**, *13*, 741. [CrossRef]
44. Chen, X. Experimental and Theoretical studies of Incompatibility and Dislocation Pile-up Stresses at Grain Boundaries Accounting for Elastic and Plastic Anisotropies. Ph.D. Thesis, Université de Lorraine et Université de Saarbrücken, Metz, France, 2020.
45. Suzuki, T.; Takeuchi, S. Correlation of Peierls-Nabarro Stress with Crystal Structure. *Rev. Phys. Appl.* **1988**, *23*, 685–685. [CrossRef]
46. Kheradmand, N. Grain Boundary-Dislocation Interaction: A local Investigation via Micron-Sized Bicrystals. Ph.D. Thesis, Universität des Saarlandes, Saarbrücken, Germany, 2012.
47. Wagoner, R.H. Calculating dislocation spacings in pile-ups at grain boundaries. *Metall. Trans. A* **1981**, *12*, 2015–2023. [CrossRef]